RSC Advances

PAPER

View Article Online
View Journal | View Issue

Cite this: *RSC Adv.*, 2022, **12**, 8502

Structural characteristics, cation distribution, and elastic properties of Cr^{3+} substituted stoichiometric and non-stoichiometric cobalt ferrites†

M. A. Islam, *[a] A. K. M. Akther Hossain, [a] M. Z. Ahsan, [b] M. A. A. Bally,[a] M. Samir Ullah,[a] S. M. Hoque [c] and F. A. Khan[a]

Structural, elastic and cation distribution properties have been investigated on stoichiometric and non-stoichiometric cobalt ferrites. Crystal structure, formation of spinel type ferrite, chemical bonding, cation distribution, and thermal properties of two series of Cr^{3+} substituted stoichiometric and non-stoichiometric various cobalt ferrites with general formula $Co_{1-x}Cr_xFe_2O_4$ (S1), and $Co_{1+x}Cr_xFe_{2-x}O_4$ (S2) were reported. Samples are synthesized by the solid-state reaction technique *via* planetary ball milling. X-ray diffraction (XRD) analysis confirms the formation of a single phase cubic spinel structure with the space group $Fd\bar{3}m$. Rietveld refinement results show that Cr occupies both the tetrahedral (A-site) and octahedral sites (B-site). The experimental lattice parameters show increasing trends for both the series with increase of Cr content. The cation–anion vacancies, chemical bonding, and the displacement of oxygen have been evaluated to understand the effect of Cr substitution and how the non-stoichiometry affects the physical and chemical properties of the material. The crystallite size is found to be the decreasing value with an increase of Cr concentration for both series of samples. Specific vibrational modes from the FTIR spectra suggest a gradual change of inversion of the ferrite lattice with the increase of Cr concentration which is also evident from Rietveld refinement data. The elastic properties analysis reveals that the synthesized samples for both series are ductile in nature. The non-stoichiometric structure with excess Co^{2+} may pave a new way to realize the lowering of Curie temperature of ferrite that is expected to improve the magnetocaloric properties.

Received 15th December 2021
Accepted 17th January 2022

DOI: 10.1039/d1ra09090a

rsc.li/rsc-advances

1. Introduction

Ferrites are ferrimagnetic materials usually used in high density recording media and satellite communication as well as microwave devices in electronic industries due to their ease of fabrication, low cost, moderate saturation magnetization, mechanical strength, and chemical stability.[1] In the last decade, the synthesis of spinel ferrites emerged extensively due to their diversified use in technological applications.[2,3] In particular, cobalt ferrite (COF) has got enormous importance both in technological as well as biomedical applications.[3–13] Intensive studies on COF have been carried out with varying doping and/or substituting the divalent or trivalent cations and synthesizing them by different methods.[3,14,15] In order to confirm the crystallinity and the phase of the synthesized materials, Rietveld refinement has been significantly used on the X-ray diffraction (XRD) data of the samples.[1,9–11,16] Amri *et al.*[1] have calculated the theoretical lattice parameters along with hopping lengths, oxygen positional parameters, cation–cation and cation–anion bond lengths of Ni–Zn–Al ferrite. Kumar *et al.*[14] have reported on the estimation of the lattice parameters by using Nelson–Riley (N–R) function, intrinsic strain and crystallite size by using Williamson–Hall (W–H) method. It has also been studied that the crystallite size and intrinsic strain can be determined from the XRD peak broadening analysis by using several ways such as W–H method, size strain plot (SSP), Scherer method, and the modified Scherer method (MS).[14,17,18] However, it is reported that SSP and MS methods are found more significant compared to that of W–H and Scherer methods, because both SSP and MS can be observed at a lower angle where the accuracy is found to be very high.[18] On the other hand, the formation of ferrite and identification of the chemical bonds can be analyzed from the Fourier transform infrared (FTIR) spectra.[1,19–21] Several techniques for the measurement mechanical properties have been used to calculate the elastic and mechanical properties. FTIR is one of the suitable techniques found to calculate the elastic and thermal properties. The elastic moduli, Debye

[a]*Department of Physics Bangladesh University of Engineering and Technology, Dhaka 1000, Bangladesh. E-mail: maislam.buet.phy@gmail.com*

[b]*Departments of Chemistry and Physics, Gono Bishwabidyalay, Savar, Dhaka-1344, Bangladesh*

[c]*Materials Science Divisions, Atomic Energy Center, Dhaka-1000, Bangladesh*

† Electronic supplementary information (ESI) available. See DOI: 10.1039/d1ra09090a

temperature, and minimum thermal conductivity can be calculated by using stiffness, lattice parameters, and X-ray density which have been reported in various literatures[1,19,20,22] Chandekar, *et al.*[22] reported the corrected zero porosity elastic moduli estimated from the calculated elastic moduli and porosity.

The synthesis and characterization of ferrites have attracted increasing attention in recent years. Many efforts have been attempted to expand potential applications by improving their properties. Research on inorganic compounds with a non-stoichiometric ratio is a great challenge. Andersen *et al.*[23] reported the local and long-range magnetic structure of non-stoichiometric nanocrystalline spinel type iron oxide. They have found the vacancy ordering in the structure which reveals the shorter coherence length on the non-stoichiometric spinel type iron oxide. In addition various literature on non-stoichiometric compounds have been found,[24–28] where remarkable effects of non-stoichiometry on structural, and magnetic properties have been presented.

This study focuses on how Cr^{3+} affect the structure of stoichiometric COF with the formula $Co_{1-x}Cr_xFe_2O_4$ (S1) and non-stoichiometric COF having the formula $Co_{1+x}Cr_xFe_{2-x}O_4$ (S2), where $x = 0.125$, 0.25, 0.375, and 0.50. The cation distribution has been calculated using site occupancy data extracted from the Rietveld refined XRD data. Besides, the theoretical and experimental lattice parameters, oxygen positional parameter, tolerance factor, ionic packing coefficient, vacancy parameter, bond lengths, bond angles, density, and porosity of the above-mentioned samples of both the series have been determined. Crystallite size estimation by various methods such as W–H, SSP, Scherer, MS, and Rietveld methods has also been explained in this study. FTIR spectra have been illustrated to confirm the ferrite formation for the samples of both the investigated series. In addition, elastic and thermal properties have also been explained from the FTIR and structural data. A correlation between the elastic properties and structural properties has been established for exploiting their advanced applications. The main focus of this work is to find the structural defects of COF with Cr^{3+} substitution at the Co^{2+} site. In addition, effects of non-stoichiometry on the structure of COF are also explored.

2. Experimental procedure

2.1 Synthesis technique

The selected two series of stoichiometric and non-stoichiometric COF denoted as S1 and S2 have been synthesized by the standard solid-state reaction method. The required amount of Co_2O_3 (98.0%), Cr_2O_3 (99.9%), and Fe_2O_3 (96.0%) are weighed in an analytical balance and hand mixed in a mortar pestle for 2 h. The mixed powders are milled in a planetary ball mill (MSK-SFM-1) for 12 h. The milled powders are calcined at 800 °C for 6 h for a complete solid-state reaction through diffusion of particles. Then the powders of each composition are pressed into pellets by applying a hydraulic pressure of 16 000 psi. Finally, the pellets are sintered at 1200 °C for 6 h in a furnace and rcrushed in to fine powders.

2.2 Characterizations

The X-ray diffraction (XRD) data of the synthesized samples are taken using a Rigaku Smart Lab X-ray diffractometer with Cu-Kα radiation ($\lambda = 1.5406$ Å) with the scanning angle 2θ within the range of 10 to 80°. The Rietveld refinement was carried out using the Full-Prof software integrated in Match-3 software. Room temperature Fourier transform infrared (FTIR) spectroscopy (Spectrometer model-IR Prestige-21) in the region 350–4000 cm^{-1} was used to find out the functional groups and vibrational structure of the synthesized samples. The parameters related to structural, elastic, and thermal properties are calculated using the XRD data and FTIR spectra.

3. Results

3.1 XRD analysis

The X-ray diffraction patterns along with Rietveld refined data have been shown in Fig. 1, 2, and 3 for the parent COF, other samples of the series S1, and S2, respectively. XRD pattern of the parent COF satisfy the Bragg's condition at 2θ values of 30.37°, 35.76°, 43.4°, 53.84°, 57.4°, and 62.92° with corresponding crystal planes are indexed with (220), (311), (400), (511), and (440), respectively. These sharp peaks, corresponding to the aforesaid (*hkl*) planes indicate a single phased inverse spinel structure with space group $Fd\bar{3}m$ of parent COF that has been confirmed by the crystallography open database (COD No. 5910063) as reported in the literature.[29] No impurity phase has been observed in the pattern for the parent COF which signifies the phase purity of COF. The XRD patterns for the samples of the stoichiometric series S1 and non-stoichiometric series S2 shown in Fig. 2 and 3, reveal the formation of spinel structure (COD No. 910063). The peak positions of (311) plane for both the series S1 and S2 have been shifted towards the lower 2θ angle with an increase of Cr content as shown in Fig. 2(b) and 3(b), which imply an increase of the lattice parameters as a result of Cr substitution.

3.1.1 Estimation of cation distribution. The cation distribution of the samples at the tetrahedral and octahedral sites of

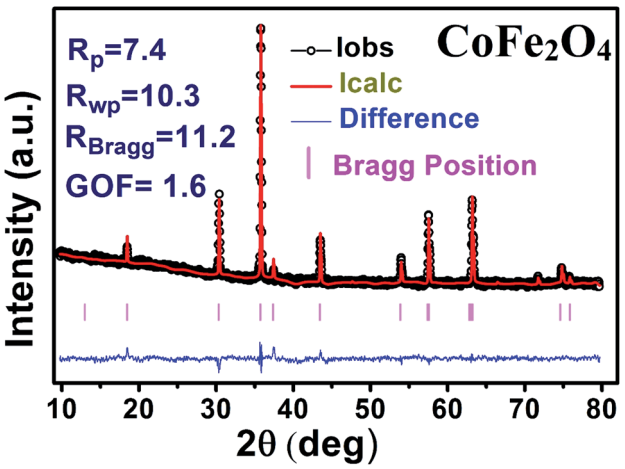

Fig. 1 Rietveld analysis of XRD pattern of $CoFe_2O_4$.

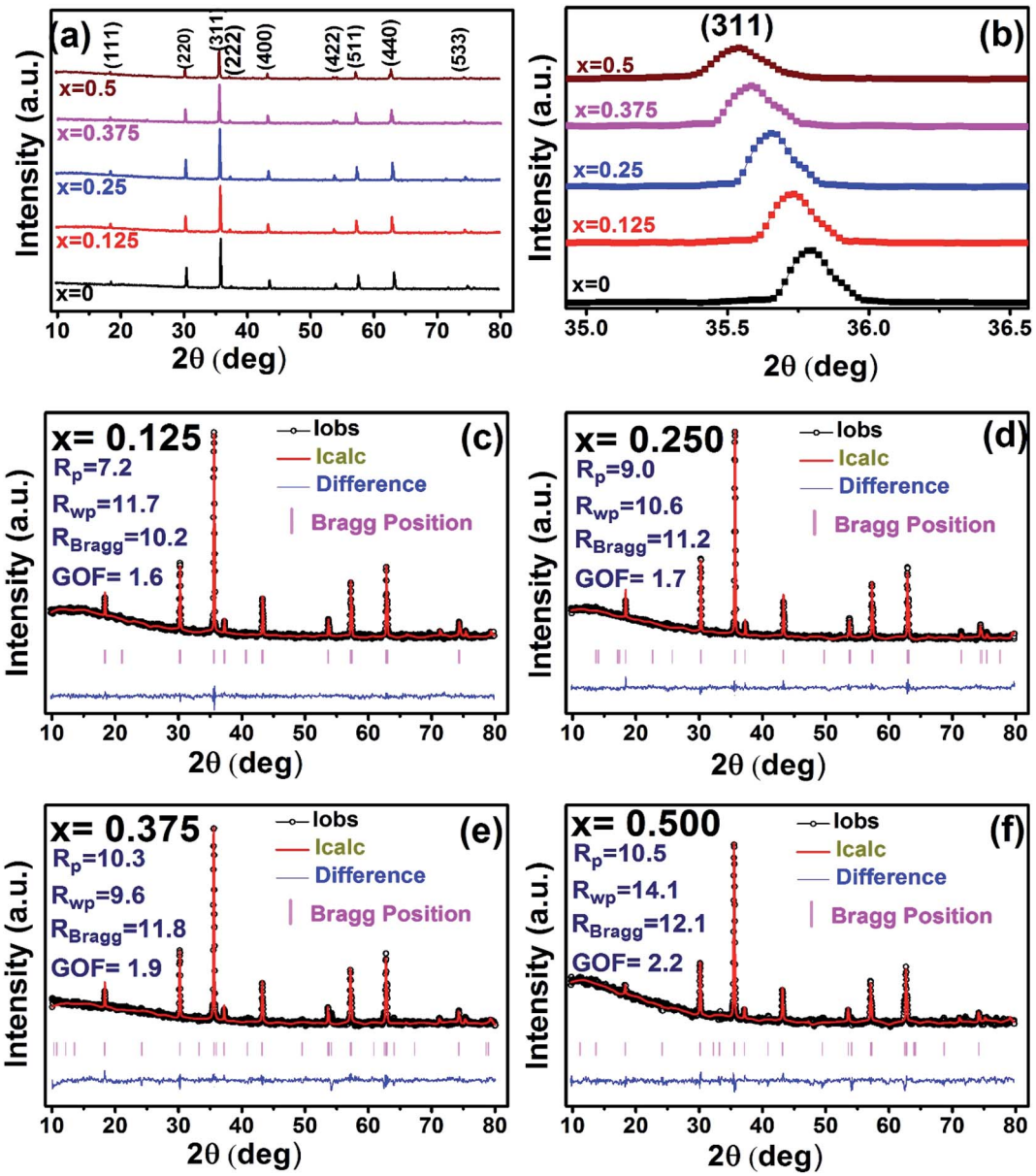

Fig. 2 Rietveld analysis of XRD patterns for all samples of S1 ($Co_{1-x}Cr_xFe_2O_4$) series.

spinel structure has been determined by comparing the observed X-ray intensities from the specific planes of (220), (440), (400), and (422). The ratios of observed and calculated intensities *viz.* I_{220}/I_{400}, I_{220}/I_{440}, I_{422}/I_{440}, and I_{400}/I_{440} are considered to evaluate the cation distribution. From the calculation of structure factor, it is reported that (220) and (440) are sensitive to cation distribution at the tetrahedral site, while (400) and (422) are sensitive to cation distribution at the octahedral site.[30] The general formulae for cation distribution at the tetrahedral site and octahedral site for samples of the series S1, and S2, are as follows:

Possible cation distribution of S1 series is

$$[Co_\alpha Cr_\beta Fe_\gamma]^{tet}[Co_{1-x-\alpha}Cr_{x-\beta}Fe_{2-\gamma}]^{oct}O_4$$

Possible cation distribution of S2 series is

$$[Co_\alpha Cr_\beta Fe_\gamma]^{tet}[Co_{1+x-\alpha}Cr_{x-\beta}Fe_{2-x-\gamma}]^{oct}O_4$$

where α,β, and γ are the cationic parameters for the tetrahedral site and $\alpha + \beta + \gamma = 1$. For COF $x = \beta = 0$. The cation distribution has been calculated by the above formulae and tabulated in Table 1. The value of the inversion parameter as determined by calculating the ratio between Fe^{3+} at the tetrahedral site and Fe^{3+} at octahedral site Fe_{tetra}/Fe_{octa} has also been tabulated in Table 1. Using the exact cation distribution the ionic radius for the tetrahedral site (r_{tet}), and octahedral site (r_{oct}), have been calculated by the following relations:[16]

$$r_{tet} = \alpha r_{Co} + \beta r_{Cr} + \gamma r_{Fe} \text{ for both the series,}$$

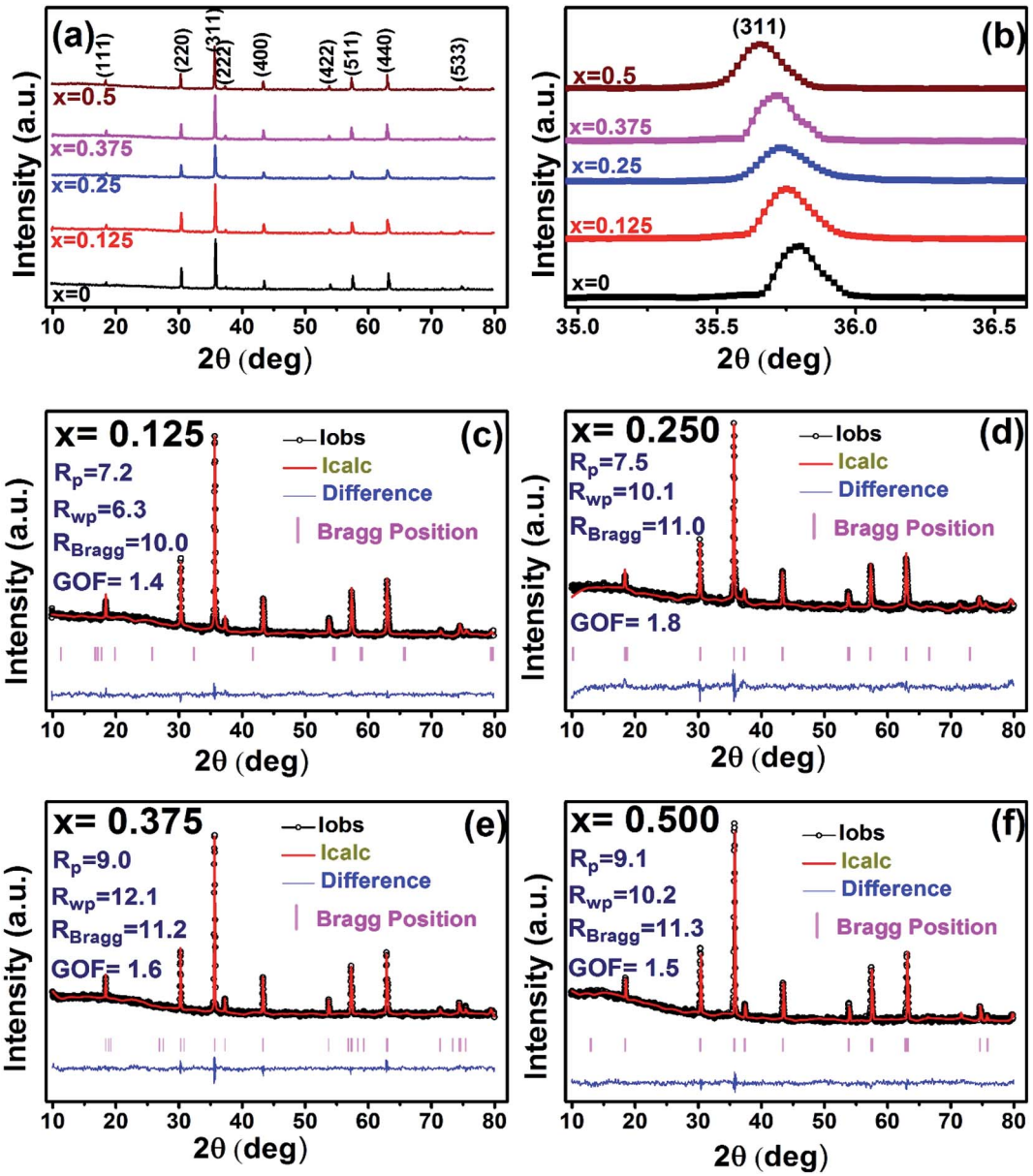

Fig. 3 Rietveld analysis of XRD patterns for all samples of S2 ($Co_{1+x}Cr_xFe_{2-x}O_4$). series.

$$r_{oct} = 0.5 \times \{(1 - x - \alpha)r_{Co} + (x - \beta)r_{Cr} + (2 - \gamma)r_{Fe}\} \text{ for S1,}$$

$$r_{oct} = 0.5 \times \{(1 + x - \alpha)r_{Co} + (x - \beta)r_{Cr} + (2 - x - \gamma)r_{Fe}\} \text{ for S2,}$$

where r_{Co}, r_{Cr}, and r_{Fe} are the ionic radii of Co^{2+}, Cr^{3+}, and Fe^{3+}, respectively. The calculated ionic radii for the tetrahedral site and octahedral site are tabulated in Table 1.

Fig. 4 represents the Energy Dispersive (EDS) spectra for all samples. The elemental analysis are performed from these spectra. From the data of EDS spectra, it is confirmed that chemical composition of the synthesized samples are close to the respective nominal composition.

3.1.2 Lattice parameter estimation. To determine true value of lattice parameter (a_{true}) from XRD data, Nelson–Riley (N–R) extrapolating function (eqn (A2)) has been used.[17] The lattice parameter for each Bragg position has been calculated using eqn (A3). The N–R function *vs.* a_{hkl} graph has been plotted for each sample which is shown in Fig. 5 for both the series S1 and S2, respectively. From Fig. 5 the true value of lattice parameters for each sample have been determined by extrapolating $\theta = 0°$. The extracted value of a_{true} for each sample have been illustrated in Fig. 6. The lattice parameters calculated from the XRD data by using Match-3 software are denoted by a_{exp}, and these values for the both series of samples have been illustrated in Fig. 6. The lattice parameters calculated using the eqn (A1) are denoted by a_{th}, and these values also have been illustrated in Fig. 6. It is observed that a_{exp} for the sample of both series follows the similar increasing trend of the a_{th} and a_{true} with the Cr content which implies that a_{exp} is reliable. This increase in lattice parameter for S1 series may be caused due to

Table 1 Possible cation distribution for all samples of series S1 ($Co_{1-x}Cr_xFe_2O_4$) and S2 ($Co_{1+x}Cr_xFe_{2-x}O_4$)

Series		S1				S2				
x		0.000	0.125	0.250	0.375	0.500	0.125	0.250	0.375	0.500
Tetrahedral site(±2%)	Co	0.132	0.100	0.090	0.070	0.050	0.179	0.121	0.042	0.012
	Cr	0	0.057	0.110	0.166	0.232	0.011	0.012	0.018	0.008
	Fe	0.868	0.843	0.800	0.764	0.718	0.810	0.867	0.940	0.980
Octahedral site (±2%)	Co	0.868	0.775	0.660	0.555	0.450	0.946	1.129	1.333	1.488
	Cr	0	0.068	0.140	0.209	0.268	0.114	0.238	0.357	0.492
	Fe	1.132	1.157	1.200	1.236	1.282	1.065	0.883	0.685	0.520
Calculated	I_{400}/I_{440}	0.77	0.76	0.81	0.81	0.83	0.83	0.85	0.80	0.80
	I_{220}/I_{440}	0.98	0.82	1.11	1.05	1.06	1.14	1.08	1.05	0.80
Observed	I_{400}/I_{440}	0.74	0.75	0.72	0.76	0.78	0.84	0.90	0.78	0.77
	I_{220}/I_{440}	1.03	1.03	1.10	1.02	1.01	1.25	1.24	1.00	1.04
Inversion parameter (y)		0.76	0.72	0.66	0.62	0.56	0.76	0.98	1.37	1.88
Ionic radius (Å)	r_{tet}	0.63	0.64	0.65	0.66	0.68	0.64	0.63	0.62	0.61
	r_{oct}	0.69	0.68	0.68	0.67	0.66	0.73	0.78	0.83	0.87

the larger ratio of Cr^{2+}/Co^{2+} at tetrahedral site than the Cr^{3+}/Co^{2+} ratio at octahedral site. The increasing trends of lattice parameter for S2 are due to the excess Co^{2+} with an ionic radius of 0.75 Å which is larger than that of Cr^{3+} (0.63 Å).[31] Since unit cell volume is directly proportional to the lattice constant, hence it follows a similar trend of the lattice constant.

3.1.3 Density and porosity estimation. The bulk density d_B, crystal density d_x, and porosity (P) for both series of samples have been calculated using eqn (A4), (A5), and (A6), respectively and have been illustrated as a function of Cr concentration in Fig. 7. The density extracted from the Rietveld refined data is denoted as d_{reit} is also presented in Fig. 7. These parameters have been listed in Table 2. It is seen that the d_x, and d_B show a similar decreasing trend with the increase in Cr content which agrees with the Rietveld refined density d_{reit}. The decreasing trend of the density is due to the molecular weight loss of the investigated samples. Furthermore, it is seen that the d_x and d_B follow the increasing trend with the Cr content that is also agrees with the d_{reit} for the samples of the series S2. This increasing nature of density may have been caused by the molecular weight gain due to the non-stoichiometry of samples of the series S2. The porosity is found to increase with the addition of Cr content for the samples of both series.

3.1.4 Oxygen positional parameter, interionic distance and bond angle estimation. When tetrahedral interstices are occupied by divalent ion then the expansion in tetrahedral site is relatively larger than octahedral site due to the difference of ionic radii of cations. This expansion can be explained by oxygen positional parameter, u, which gives quantitative measure of the displacement of oxygen ions. This displacement takes place whenever there is a difference in the radii of substituted and replaced ions. The value of u can be calculated from the a_{th} using the eqn (A7).

The calculated u values for both series are listed in Table 4. As seen in that table, u value is almost invariant with Cr content for both series found to be almost equal to that of the parent COF. In a cubic spinel structure the ideal value of u is equal to 3/8 = 0.375. The calculated value of u is slightly larger than that of ideal value, which may be due to the anion displacement from its ideal position. From the analysis of u and δ ($= u - 0.375$), it is confirmed that lattice is slightly distorted for all the samples of both series.[33]

The inter-ionic distance between magnetic ions is named as hopping length in tetrahedral site (L_A) and octahedral site (L_B) which gives information about the strength of spin interaction of ions. The hopping lengths have been calculated by using Stanley's equations (eqn (A8)).[1] The calculated values of L_A and L_B have been tabulated in Table 3 for both the series. Hopping lengths decrease for S1 series, and increase for S2 series with the increasing Cr content.

The tetrahedral and octahedral bond lengths (d_{AL}) and (d_{BL}), tetrahedral edge length (d_{AE}), and shared octahedral edge lengths (d_{BE}) and un-shared lengths (d_{BEU}) have been calculated using eqn (A9)–(A13). The calculated d_{AL}, d_{BL}, d_{AE}, $d_{BE,}$ and d_{BEU} values for both the series have been listed in Table 3. From this Table, it is seen that the values of d_{AL}, d_{AE} have increased while the values of d_{BL}, $d_{BE,}$ and d_{BEU} have reduced with an increase in Cr content for both the series S1, and S2.

Magnetic interaction strength for cubic spinel and spinel-like ferrite depends on the cation–cation (Me–Me) bond length and cation–anion (Me–O) bond length and bond angle that have been calculated using the eqn (A14)–(A27). All the calculated bond lengths and bond angles have been presented in Table 3. As seen in Table 3, there is decreasing and increasing trend in Me–Me for the S1 and S2 series, respectively. The Me–O distance shows an increasing trend for both the series. The bond angles show a decreasing trend with the increasing Cr content for both series. The decreasing trend of Me–Me and the bond angles may be due to the smaller ionic radius of Cr^{3+} than that of the Co^{2+} for the samples of the series S1. But in the case of the samples of series S2, this decreasing in Me–Me and bond angles is most likely due to the combined effects of smaller ionic radius of Cr^{3+} and excess of Co^{2+} ions therein. This behavior of bond length and bond angles for the samples of the series S1, and S2 imply the lattice expansion with the increase in Cr content, which is found to be in agreement with the lattice volume.

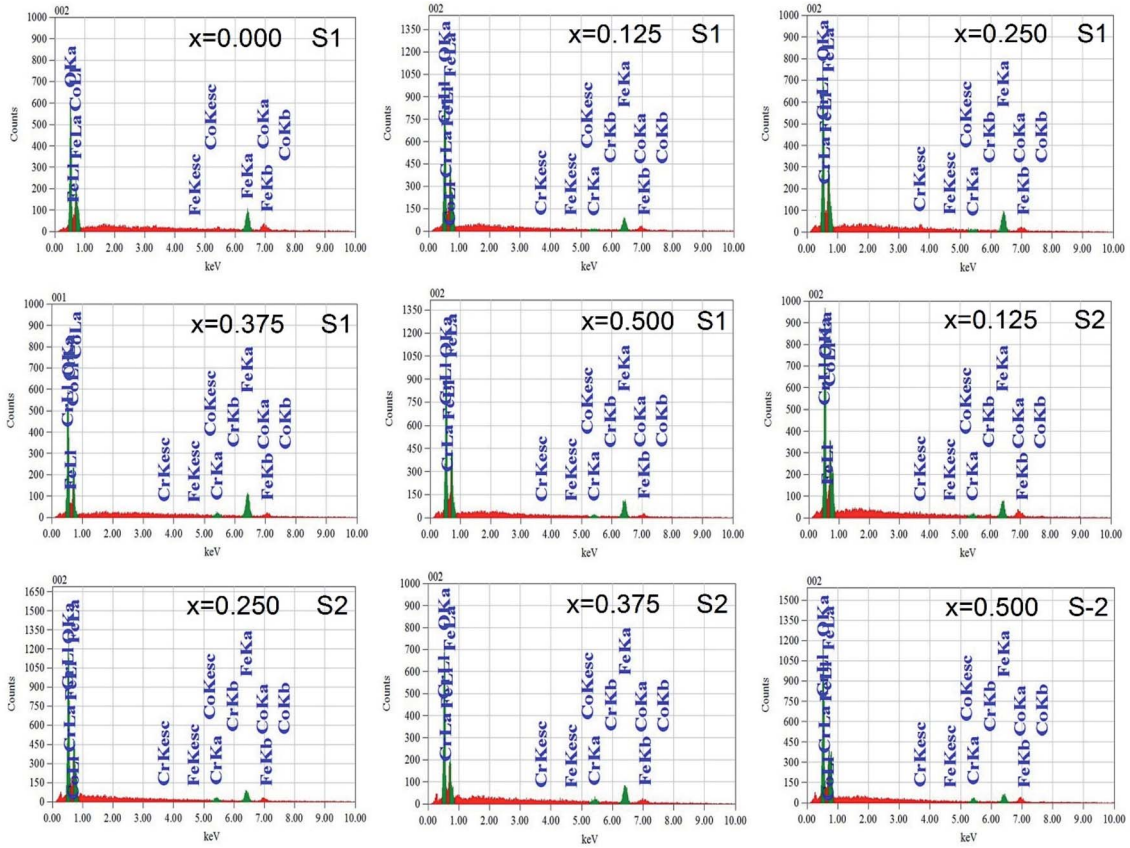

Series	x	Table for Mass (%)							
		From formula mass				From EDX analysis			
	Elements	Co	Cr	Fe	O	Co	Cr	Fe	O
S1	0	25.12	0	47.60	27.27	27.37	45.51	0	26.12
	0.125	22.06	2.78	47.78	27.37	23.03	47.42	2.82	16.73
	0.25	18.98	5.58	47.96	27.47	18.59	45.73	5.2	30.49
	0.375	15.87	8.40	48.14	27.58	17.37	49.82	7.67	25.13
	0.5	12.74	11.24	48.32	27.68	13.15	49.77	12.54	24.54
S2	0.125	27.45	2.69	43.36	26.49	18.19	43.73	2.12	25.26
	0.25	29.65	5.23	39.34	25.76	18.81	39.49	4.57	27.13
	0.375	31.74	7.63	35.55	25.07	30.42	38.81	7.55	23.23
	0.5	33.72	9.91	31.95	24.41	32.06	32.25	9.38	26.31

Fig. 4 EDX spectra of all samples of S1 ($Co_{1-x}Cr_xFe_2O_4$) and S2 ($Co_{1+x}Cr_xFe_{2-x}O_4$). series with mapping of compositions.

To confirm the presence of cation or anion vacancies, estimation of ionic packing coefficient is required. The ionic packing coefficient of tetrahedral site P_{tet} and octahedral site P_{oct} have been calculated by the eqn (A28) and (A29), respectively. The values for P_{tet} and P_{oct} have been presented in Table 4 for both the series. From Table 4, it is observed that the values of P_{tet} and P_{oct} are less than one, which suggests the existence of cation and anion vacancies in the parent COF.[34] For series S1, the values of P_{tet} and P_{oct} increase for increasing Cr content and the values are close to 1, which indicates the reduction of ion (cation and anion) vacancies. On the other hand, P_{tet} and P_{oct} have been found to be decrease with increasing Cr^{3+} content which indicates enhancement of ion (cation and anion) vacancies.

The degree of ionic packing coefficient can be evaluated by calculating the fulfillment coefficient (α) of the unit cell using eqn (A30). The vacancy parameter β is defined as normalized values of ions at the nodal point of the spinel structure which is calculated using eqn (A31). The values of α (tabulated in Table 4) show close to 0.58 for all the samples which confirm that our synthesized samples exhibit inverse spinel structure as explained in the earlier literature.[34] The values of β listed in Table 4 show a low vacancy parameter which implies that the missing ions are lesser for parent COF. For series S1 the values

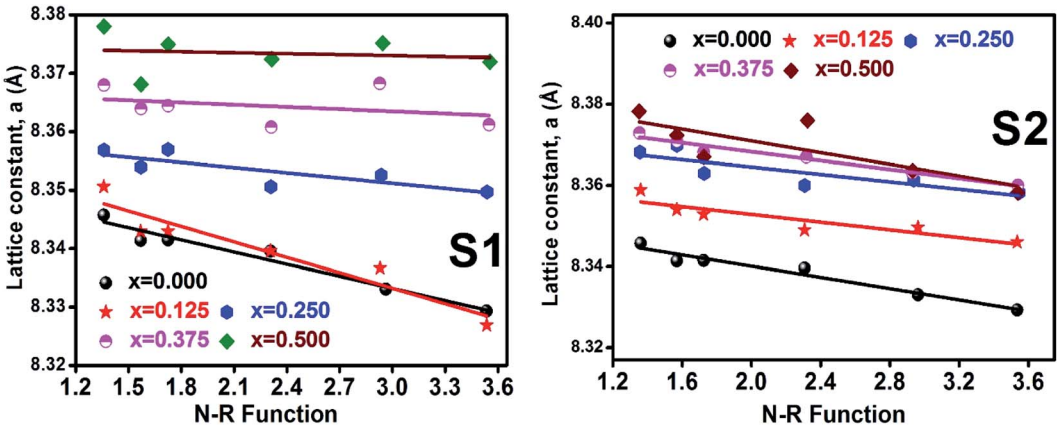

Fig. 5 Nelson–Riley plot for all samples of series S1 ($Co_{1-x}Cr_xFe_2O_4$) and S2 ($Co_{1+x}Cr_xFe_{2-x}O_4$).

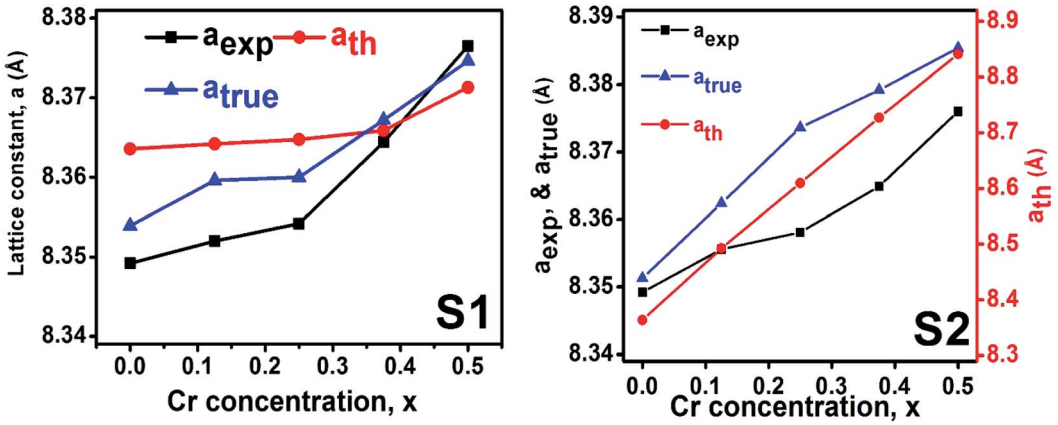

Fig. 6 Lattice constants as function of Cr content for all samples of series S1 ($Co_{1-x}Cr_xFe_2O_4$) and S2 ($Co_{1+x}Cr_xFe_{2-x}O_4$).

of β shows the decreasing trend up to $x = 0.375$ that implies reducing the missing ions due to Cr substitution. But at higher Cr content, it shows the negative value, which are most likely due to the excess of ions. The excess of ions dominates due to higher Cr content in series S1. But in series S2, β values increase strongly with an increase of Cr content that dominates the enhancement of metallic behavior from semiconducting behavior due to the higher values of Co^{2+} ions.[35]

The tolerance factor (T) is another property to get an idea about the impurities of these type of materials. Hence the T have been calculated using eqn (A32) that have been tabulated in Table 4 for both the series. It is observed that T is slightly

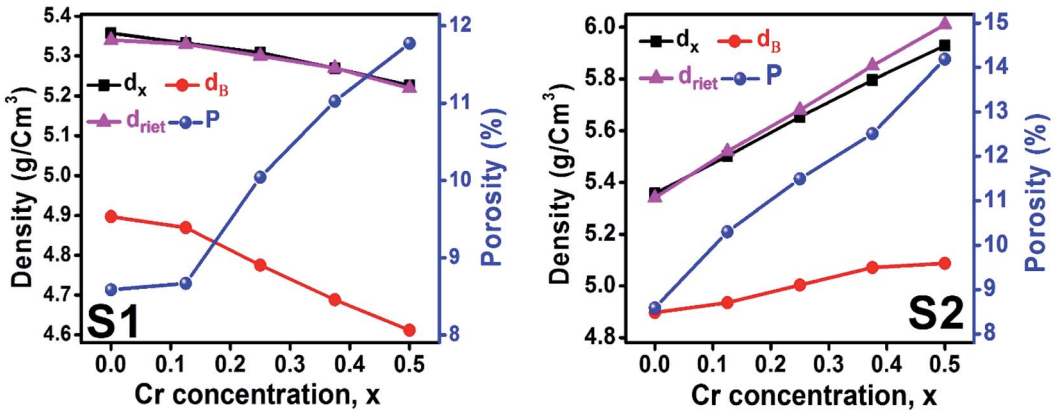

Fig. 7 Density and porosity as function of Cr content for all samples of series S1 ($Co_{1-x}Cr_xFe_2O_4$) and S2 ($Co_{1+x}Cr_xFe_{2-x}O_4$).

Table 2 Lattice parameter, density, and porosity for all samples of series S1 ($Co_{1-x}Cr_xFe_2O_4$) and S2 ($Co_{1+x}Cr_xFe_{2-x}O_4$)

Series	x	a_{exp} (Å)	V_{exp} (Å^3)	a_{true} (Å)	V_{true} (Å^3)	a_{th} (Å)	V_{th} (Å^3)	d_x (g cm^{-3})	d_B (g cm^{-3})	d_{reit} (g cm^{-3})	P (%)
S1	0	8.3492	582.01	8.3539	582.45	8.3635	585	5.36	4.90	5.34	9
	0.125	8.3520	582.6	8.3596	579.51	8.3642	585	5.33	4.87	5.33	9
	0.250	8.3542	583.06	8.3600	578.15	8.3647	585	5.31	4.78	5.29	10
	0.375	8.3644	585.2	8.3672	577.47	8.3658	586	5.27	4.69	5.27	11
	0.500	8.3765	587.74	8.3746	576.55	8.3713	587	5.31	4.61	5.22	13
S2	0.125	8.3556	582.39	8.3705	586.48	8.4927	613	5.52	4.94	5.52	11
	0.250	8.3581	589.32	8.3896	590.50	8.6096	638	5.67	5.00	5.68	12
	0.375	8.3649	595.80	8.3958	591.81	8.7272	665	5.82	5.07	5.85	13
	0.500	8.376	604.68	8.4061	593.99	8.8414	691	5.95	5.09	6.01	15

Table 3 Values of hopping lengths (L_A, L_B), tetrahedral bond length (d_{AL}), octahedral bond lengths (d_{BL}), tetrahedral edge length (d_{AE}), shared and unshared octahedral edge (d_{BE}, d_{BEU}), interatomic bond lengths and angles for all samples of series S1($Co_{1-x}Cr_xFe_2O_4$) and S2 ($Co_{1+x}Cr_xFe_{2-x}O_4$)

Series		S1					S2			
x		0.000	0.125	0.250	0.375	0.500	0.125	0.250	0.375	0.500
L_A (Å)		3.623	3.622	3.617	3.616	3.614	3.667	3.717	3.768	3.809
L_B (Å)		2.958	2.957	2.953	2.952	2.951	2.994	3.035	3.077	3.11
d_{AL} (Å)		1.945	1.956	1.968	1.982	1.998	1.926	1.893	1.86	1.832
d_{BL} (Å)		2.011	2.006	2.000	1.996	1.993	2.023	2.042	2.063	2.083
d_{AE} (Å)		3.176	3.194	3.215	3.237	3.263	3.145	3.091	3.037	2.991
d_{BE} (Å)		2.727	2.711	2.692	2.677	2.659	2.762	2.818	2.877	2.931
d_{BEU} (Å)		2.956	2.958	2.959	2.964	2.969	2.957	2.956	2.958	2.961
Me–Me distances (Å)	b	2.9569	2.9572	2.9574	2.9577	2.9597	3.0026	3.0439	3.0855	3.1259
	c	3.4673	3.4676	3.4678	3.4683	3.4705	3.5209	3.5693	3.6181	3.6654
	d	3.6215	3.6218	3.6220	3.6225	3.6248	3.6774	3.7280	3.7789	3.8284
	e	5.4322	5.4327	5.4330	5.4337	5.4373	5.5162	5.5921	5.6684	5.7426
	f	5.1216	5.1220	5.1223	5.1230	5.1263	5.2007	5.2723	5.3442	5.4142
Me–O distances (Å)	p	2.0113	2.0056	1.9987	1.9923	1.9861	2.0543	2.1027	2.1523	2.1990
	q	1.9484	1.9588	1.9712	1.9829	1.9973	1.9579	1.9500	1.9405	1.9337
	r	3.7310	3.7508	3.7745	3.7970	3.8245	3.7491	3.7340	3.7158	3.7028
	s	3.6674	3.6711	3.6754	3.6797	3.6865	3.7171	3.7567	3.7959	3.8349
Bond angles (degree)	θ_1	122.23	122.00	121.74	121.49	121.21	122.67	123.41	124.17	124.85
	θ_2	140.27	139.39	138.35	137.40	136.35	142.08	145.27	148.86	152.38
	θ_3	94.62	94.98	95.43	95.85	96.33	93.90	92.73	91.58	90.58
	θ_4	126.30	126.38	126.47	126.56	126.66	126.14	125.89	125.63	125.40
	θ_5	71.54	70.98	70.31	69.68	68.99	72.70	74.68	76.80	78.75

higher than one which indicates that the synthesized sample is slightly distorted from the inverse spinel structure. In both the series, the values of T are found to decrease with the increase of Cr content indicating the reduction of distortion from the central atom resulting the improvement of inverse spinel structure.

Table 4 Oxygen positional parameter, ionic packing coefficient, fulfillment coefficient, vacancy parameter, and tolerance factor for all samples of series S1 ($Co_{1-x}Cr_xFe_2O_4$) and S2 ($Co_{1+x}Cr_xFe_{2-x}O_4$)

		Oxygen positional parameter, u and deviation, δ	Ionic packing coefficient					
Series	x	u	δ	P_a	P_b	Fulfillment coefficient α	Vacancy parameter β	Tolerance factor T
S1	0	0.3845	0.0095	0.9867	0.9967	0.5819	0.5145	1.038
	0.125	0.3852	0.0102	0.9877	0.9982	0.5811	0.4370	1.040
	0.250	0.3860	0.0110	0.9884	0.9988	0.5804	0.3783	1.043
	0.375	0.3868	0.0118	0.9919	0.9991	0.5782	0.0526	1.045
	0.500	0.3877	0.0127	0.9944	1.0008	0.5758	−0.1860	1.048
S2	0.125	0.3831	0.0081	0.9426	0.9589	0.5887	4.7671	1.027
	0.250	0.3807	0.0057	0.9016	0.9239	0.5972	8.5123	1.014
	0.375	0.3784	0.0033	0.8621	0.8940	0.6062	11.9433	1.000
	0.500	0.3763	0.0013	0.8259	0.8692	0.6150	14.9758	0.990

Table 5 Crystallite size (D) and strain (ε) estimated by different methods for all samples of series S1 ($Co_{1-x}Cr_xFe_2O_4$) and S2 ($Co_{1+x}Cr_xFe_{2-x}O_4$)

		Scherrer method	Modified Scherrer method	Rietveld refined method		Williamson–Hall Method		Size Strain Method	
Series	x	D (nm)	D (nm)	D (nm)	ε	D (nm)	ε	D (nm)	ε
S1	0	46	53	61	0.00092	71	0.000725	60	1.41×10^{-5}
	0.125	46	51	57	0.00085	70	0.000746	52	5.91×10^{-6}
	0.250	45	49	52	0.00071	64	0.000775	51	9.35×10^{-6}
	0.375	39	45	51	0.00058	60	0.000909	50	1.33×10^{-5}
	0.500	39	43	46	0.00046	56	0.000905	47	1.40×10^{-5}
S2	0.125	47	50	59	0.00075	67	0.000786	58	1.14×10^{-5}
	0.250	40	43	49	0.00068	52	0.000624	45	5.94×10^{-5}
	0.375	37	40	41	0.00051	43	0.000374	42	5.55×10^{-6}
	0.500	39	39	38	0.00046	43	0.000353	40	2.21×10^{-6}

3.1.5 Crystallite size estimation. To evaluate crystallite size, analysis of X-ray profiles is the most effective and easiest way. To calculate crystallite size and strain of the powdered samples various methods have been used such as: Scherrer, Modified Scherrer, Size strain plot, and Williamson–Hall plot. In every case, XRD data have generally been used because of X-ray line broadening comes out mainly from three factors: (i) instrumental effect, (ii) crystallite size, and (iii) local lattice strain. To exclude the instrumental broadening, a standard silicon X-ray powder diffraction data is recorded under the same condition and eliminated from the observed peak width. The full width at half maximum (FWHM) of all peak positions from the XRD has been estimated using a nonlinear combined curve fitting function that includes Gaussian and Lorentzian functions. The FWHM data has been calculated by using the eqn (A33). In addition, the instrumental broadening (β_i) is removed by using the eqn (A34). The values for β_i are 0.092°, 0.099°, 0.117°, 0.186°, 0.21°, and 0.208° for the (220), (311), (400), (511), and (440) peaks, respectively. The average crystallite size (D) have been calculated by using observed FWHM of the most intense peak (311) with the help of Scherrer equation (eqn (A35)). The calculated values of D using this method are listed in Table 5.

Scherrer equation is used to determine D for most intense peak, but since the constant value of cos θ is not maintained with the increase in 2θ and resulting errors in the D values. To avoid the above-mentioned errors, Monshi *et al.* in 2012 employed some modifications in the use of the Scherrer equation and introduced the following formula:[18]

$$\ln \beta = \ln\left(\frac{0.9\lambda}{D}\right) + \ln\left(\frac{1}{\cos\theta}\right)$$

To evaluate the more accurate values of D, ln β *vs.* $\ln\left(\frac{1}{\cos\theta}\right)$ the graph has been plotted for all the selected peaks. Then y-intercepts, $\ln\left(\frac{0.9\lambda}{D}\right)$, have been determined by the linear fitting on this graph using the origin software for the sample of series S1, and S2, as shown in Fig. 8. The calculated D values taking $e^{\ln\left(\frac{0.9\lambda}{D}\right)}$ for all the samples have been tabulated Table.

Scherrer and modified Scherrer methods can provide the only information about the crystallite size but not the information about the intrinsic strain of the lattice. As such, Williamson–Hall method has been utilized to calculate both D and

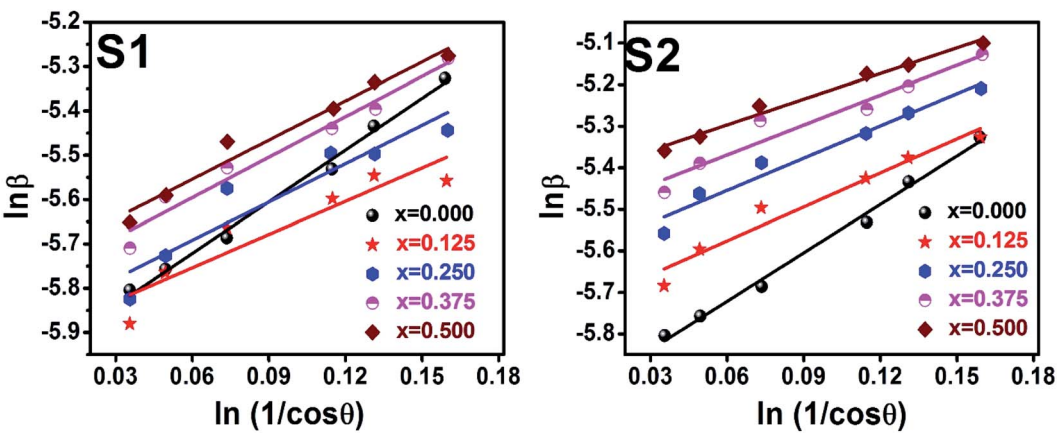

Fig. 8 Modified Scherer plots for all samples of series S1 ($Co_{1-x}Cr_xFe_2O_4$) and S2 ($Co_{1+x}Cr_xFe_{2-x}O_4$).

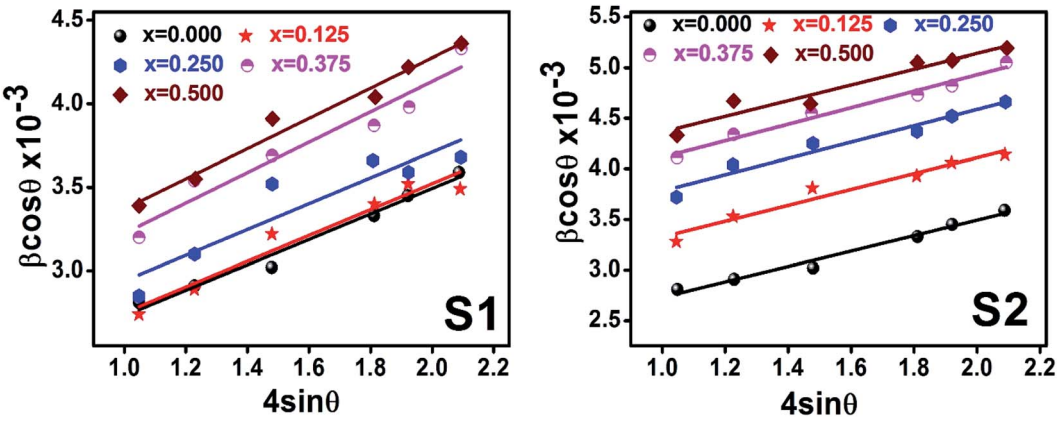

Fig. 9 Williamson–Hall Plot for all samples of series S1 ($Co_{1-x}Cr_xFe_2O_4$) and S2 ($Co_{1+x}Cr_xFe_{2-x}O_4$).

the strain, ε of the materials. According to this method, a total physical broadening, β_{tot}, have been calculated by the following relation:[14,17]

$$\beta_{tot} = \beta_{strain} + \beta_{crystal} = 4\varepsilon \tan\theta + \frac{0.9\lambda}{D\cos\theta}$$

or,

$$\beta_{hkl}\cos\theta = 4\varepsilon \sin\theta + \frac{0.9\lambda}{D}$$

Here, β_{hkl} is the total broadening due to strain and size in a particular peak having the (hkl) value which is written exchange of β_{tot}. Fig. 9 show the $\beta_{hkl}\cos\theta$ *vs.* $4\sin\theta$ graph corresponding to each diffraction peak for the samples of series S1, and S2, respectively. In every case for all the samples, the slope and y-intercept have been noted from the linear fitted curve, which gives the ε and D of the investigated samples. The ε and D for all the samples have been listed in Table 5 in Appendix B.

Williamson–Hall method describes isotropic peak broadening due to the combination of size and strain-induced effect as a function of a 2θ.To better evaluation of ε and D another model known as "size–strain plot (SSP)" has been used. In this method, higher angle reflections are less important than lower angle reflections. In the SSP method, the following relation has been considered:[17]

$$(d_{hkl}\beta_{hkl}\cos\theta)^2 = \frac{K\lambda}{D}\left(d_{hkl}{}^2\beta_{hkl}\cos\theta\right) + \frac{\varepsilon^2}{4}$$

Here, d_{hkl} is lattice spacing for different (hkl) planes. The $(d_{hkl}\beta_{hkl}\cos\theta)^2$ are plotted as a function of $d_{hkl}{}^2\beta_{hkl}\cos\theta$ and their linear fitted curve have been drawn using the origin software as shown in Fig. 10. The slope and y-intercept have been extracted for all the samples that provides the values of D and ε of both series and presented in Table 5. In addition, the D and ε values extracted by the Match-3 software from the Rietveld refined XRD data have also been listed in Table 5. The D values calculated by using all the methods is found to be decreasing trend with the increasing Cr content for both series as shown in Fig. 11. This decreasing trend is most likely due to the peak broadening.

3.2 FTIR analysis

Fig. 12 illustrate the FTIR spectrum in the wavenumber range of 350–3000 cm^{-1} for the samples of both series at room temperature. From the FTIR spectra, two distinct absorption bands at

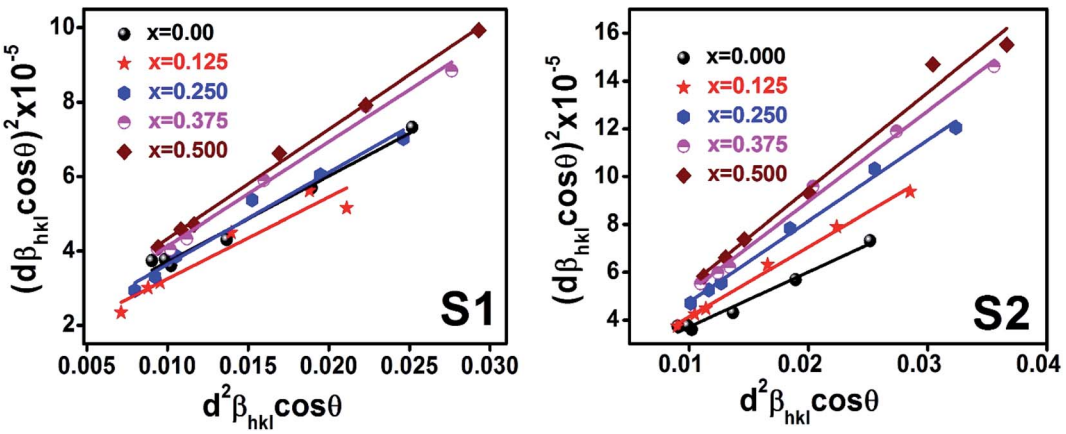

Fig. 10 Size strain plot for all samples of series S1 ($Co_{1-x}Cr_xFe_2O_4$) and S2 ($Co_{1+x}Cr_xFe_{2-x}O_4$).

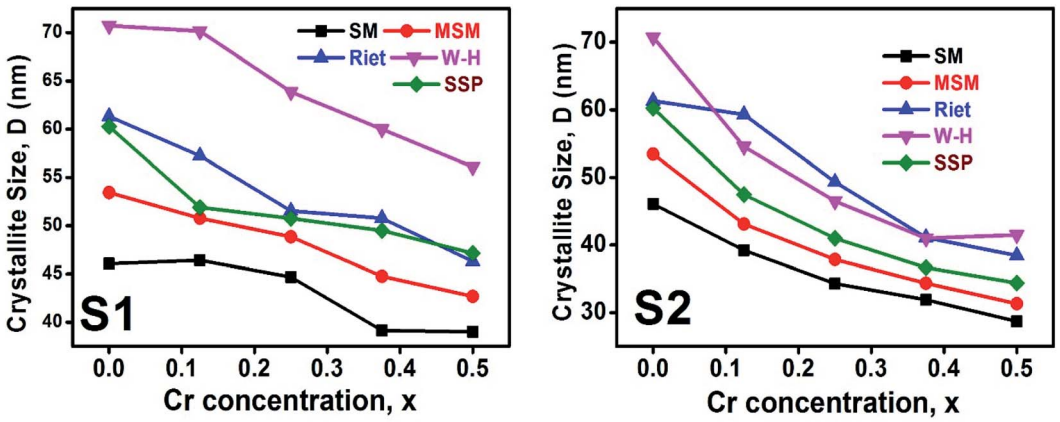

Fig. 11 The D values calculated using Scherer method (SM), modified Scherer method (MSM), Rietveld method (riet), Williamson–Hall (W–H), and size strain plot (SSP) for all samples of series S1 ($Co_{1-x}Cr_xFe_2O_4$) and S2 ($Co_{1+x}Cr_xFe_{2-x}O_4$).

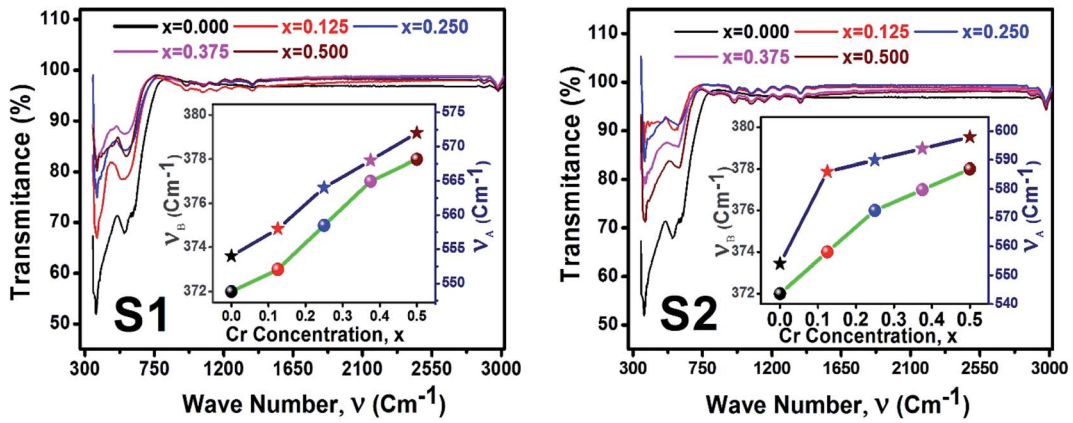

Fig. 12 FTIR spectrum for all samples of series S1 ($Co_{1-x}Cr_xFe_2O_4$) and S2 ($Co_{1+x}Cr_xFe_{2-x}O_4$).

554 cm^{-1} (ν_1) and 372 cm^{-1} (ν_2) are observed for the parent COF. The symmetrical stretching vibrations of metal–oxygen at tetrahedral and octahedral sites have been observed at the higher band ν_1, and lower band ν_2, respectively. For all samples, it is seen that both ν_1, and ν_2 are increased with the increase of Cr content as shown in the inset of Fig. 12. The values ν_1, and ν_2 have been listed in Table 6. A clear absorption band has been noticed at around 3000 cm^{-1} (ν_3). This may be attributed to the H–O–H stretching vibrations due to the effect of moisture during fabrication of the studied samples.

3.2.1. Calculation of force constant. The wavenumbers ν_1 and ν_2 of the infrared active phonon mode is directly connected to the force constant. The force constant k_t and k_o at the tetrahedral and octahedral site of cubic spinel structure has been calculated by the Waldron relation (eqn (A39)–(A41)). The average force constant $k_{av} = (k_t + k_o)/2$ have shown in Fig. 13 for the all samples of both series. From the Fig. 13, it is seen that the average force constant k_{av} increases for the samples of both series which is as usually related to the Me–Me bond distances and bond angles.

3.2.2 Elastic properties analysis. Ferrites demonstrate important elastic properties and thermal behavior due to their interatomic and interionic forces. Although the elastic properties of such materials are determined by applying external stress, according to the analysis of various research, a technique based on the structural and FTIR data parameter related to elastic properties along with thermal properties has been calculated for exploring the correlations with the other properties.[1,20–22] According to Hook's law, the stress η_i, strain $\varepsilon_{ij}$and stiffness C_{ij} are correlated on the basis of the stress–strain approach.[40] The stiffness C_{ij} are used to calculate the elastic constants. For cubic symmetry, only three stiffness C_{11}, C_{12}, and C_{44} are considered to be dominant, where C_{11} represents the elasticity in length and C_{12} and C_{44} represents the elasticity in shape. The stiffness constant C_{11} and C_{12} are calculated using eqn (A43) and (A44), and the values are tabulated in Table 6.

The bulk modulus, B, rigidity modulus, G, Young's modulus, E, Poisson's ratio, σ, longitudinal wave velocity, v_l, transverse wave velocity, v_t, and the mean velocity, v_m, have also been calculated for all samples of both series using the eqn (A46)–

Table 6 Absorbtion wave number (ν_1, ν_2), force constant, stiffness constant, wave velocity, elastic constant, Pugh ratio, Poisson ratio Debye temperature, and minimum thermal constant for all samples of series S1 ($Co_{1-x}Cr_xFe_2O_4$) and S2 ($Co_{1+x}Cr_xFe_{2-x}O_4$)

Series		S1					S2			
x		0	0.125	0.250	0.375	0.500	0.125	0.250	0.375	0.500
ν_1 (cm^{-1})		371	373	375	377	378	374	376	377	378
ν_2 (cm^{-1})		554	558	564	568	572	586	590	594	598
Force constant	k_t (N m^{-1})	290	294	300	305	309	324	329	333	338
	k_o (N m^{-1})	130	131	133	134	135	132	133	134	135
	k_{ab} (N m^{-1})	210	213	217	219	222	228	231	234	236
Stiffness costant	C_{11} (GPa)	251	255	260	264	268	273	277	280	284
	C_{12} (GPa)	105	106	106	106	106	110	110	109	108
Wave velocity	ν_l (ms^{-2})	6843	6911	6999	7080	7158	7035	6986	6940	6912
	ν_t (ms^{-2})	3950	3990	4041	4087	4133	4062	4033	4007	3991
	ν_m (ms^{-2})	4156	4197	4250	4299	4348	4272	4243	4215	4198
Elastic constant	B (GPa)	153	156	157	158	160	164	165	166	167
	G (Gpa)	84	84	87	88	89	91	92	93	95
	E (GPa)	216	220	223	226	229	234	237	239	241
Pugh ratio (B/G)		1.84	1.83	1.82	1.80	1.79	1.81	1.79	1.78	1.76
Σ		0.29	0.29	0.29	0.29	0.28	0.29	0.28	0.28	0.28
Zero porosity elastic constant	E_0 (GPa)	261	266	280	291	300	298	310	322	340
	G_0 (Gpa)	100	102	107	111	115	114	119	124	131
	B_0 (GPa)	226	230	238	244	250	252	259	265	275
σ_0		0.31	0.31	0.30	0.30	0.30	0.30	0.30	0.29	0.29
B_0/G_0		2.26	2.25	2.22	2.19	2.16	2.20	2.16	2.14	2.09
θ_D (K)		593	599	606	612	618	610	605	601	598
K_{min}		1.31	1.33	1.34	1.36	1.37	1.35	1.34	1.33	1.32

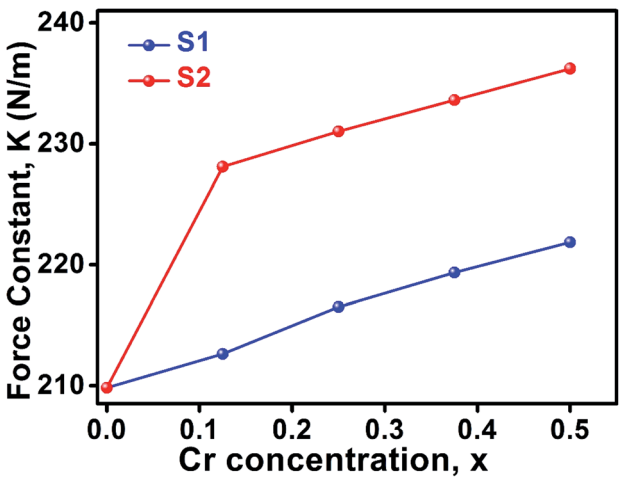

Fig. 13 Force constant as a function of Cr content all samples of series S1 ($Co_{1-x}Cr_xFe_2O_4$) and S2 ($Co_{1+x}Cr_xFe_{2-x}O_4$).

(A51). The calculated values of all these elastic constants with Cr content for both the series have been graphically presented in Fig. 14. The values of E, B, and G are found to increase with increasing Cr content. The measured elastic moduli however do not provide enough information on the mechanical properties of the investigated samples due to the presence of porosity. Hence, to improve the elastic nature of the materials, the corrected zero porosity elastic moduli have been calculated by using Hasselman and Fularth's formula (eqn (A51)–(A54)). The corrected zero porosity elastic moduli (E_0, B_0, and G_0) have been listed in Table 6 which shows the larger value than the measured E, B, and G. From Table 6, it is seen that the values of E_0, B_0, and G_0 show the similar trend with the values of E, B, and G as a function of Cr concentration for the samples of both series.

Ductility and brittleness behavior of a material can be estimated by the Pugh's ratio.[42] The Pugh's ratios (B/G) are illustrated in Fig. 15 for the samples of both series. According to Frabtsevich *et al.*[43] the brittleness and ductility nature can be confirmed from the value of σ. The calculated values of σ are also illustrated in Fig. 15. It is observed that both the Pugh's ratio and σ are higher than that of their respective critical values 1.75 and 0.26, respectively. This reveals the ductile nature of the synthesized samples.[42,43] The ductility decrease with the increase of Cr content for both the series which may be due to the substitution of brittle Cr with ductile Co and Fe for the sample of both series. In addition, σ for all the samples are in the range of 0.27–0.30 which lies in between −1 to 0.5 which implies that the investigated samples are of isotropic elastic in nature.

3.2.3 Thermodynamic properties. The Debye temperature, θ_D, is a significant parameter to know about the thermodynamic properties of a solid that originates from the maximum lattice vibration of the atoms. According to Anderson's formula the θ_D can be calculated using the eqn (A55). Thermal conductivity is one of the thermodynamic properties of a material that indicates the ability to conduct heat. The minimum value of thermal conductivity, K_{min}, have been calculated by the eqn (A56). The calculated θ_D and K_{min} have been presented in Fig. 16 as a function of Cr content for all samples of both series. It is observed that θ_D and K_{min} increases with the increase of Cr content for S1 series. However, for S2 series both θ_D and K_{min} shows the maximum value for $x = 0.125$, and beyond this value of Cr content they decrease.

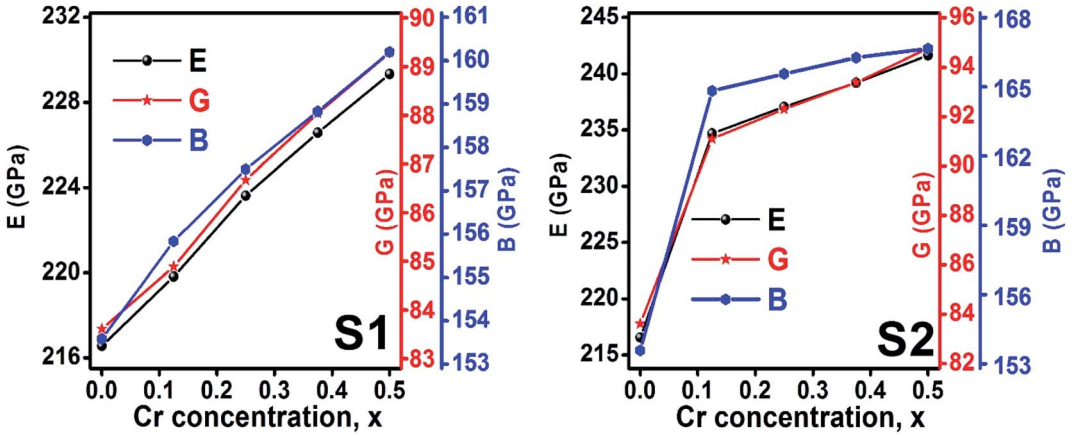

Fig. 14 Elastic modulus as a function of Cr content for all samples of series S1 ($Co_{1-x}Cr_xFe_2O_4$) and S2 ($Co_{1+x}Cr_xFe_{2-x}O_4$).

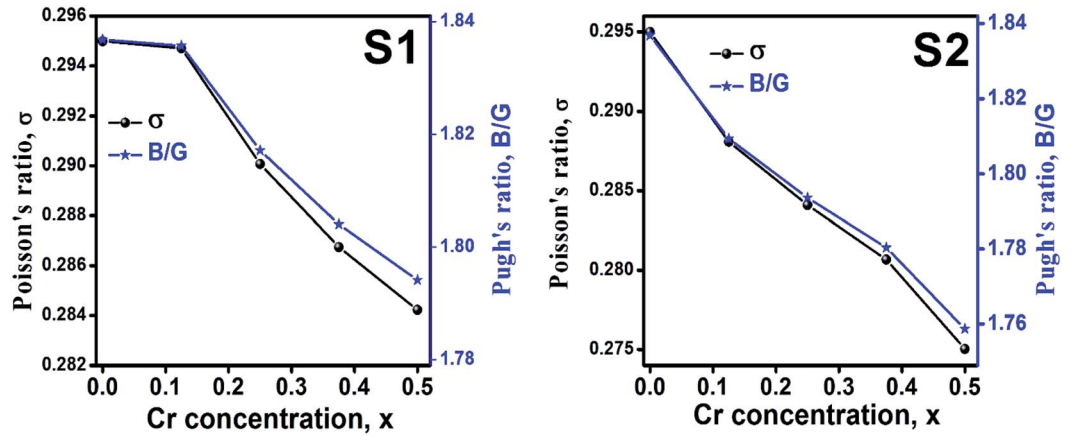

Fig. 15 Poison's ratio and Pugh's ratio as a function of Cr content for all samples of series S1 ($Co_{1-x}Cr_xFe_2O_4$) and S2 ($Co_{1+x}Cr_xFe_{2-x}O_4$).

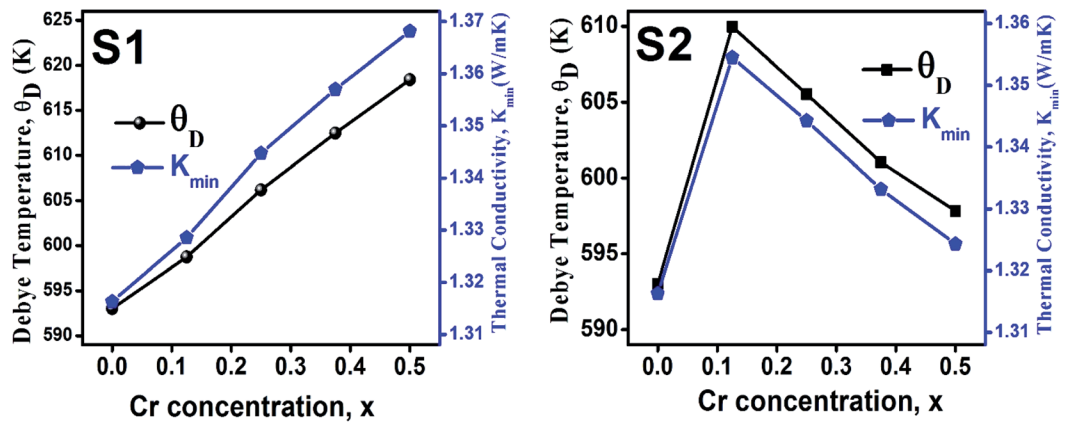

Fig. 16 Debye temperature and thermal conductivity as a function of Cr content for all samples of series S1 ($Co_{1-x}Cr_xFe_2O_4$) and S2 ($Co_{1+x}Cr_xFe_{2-x}O_4$).

4. Discussion

The analysis of structural, mechanical, and thermal properties of the samples of two series S1, and S2, show almost similar behavior in most of their properties. For the stoichiometric series S1, the XRD pattern shows a single phase cubic structure for all Cr contents. For a lower value of Cr^{3+} substitution with Co^{2+}, cation–anion vacancies dominated. However, for higher values of Cr^{3+}, negative values of vacancy parameter have been found. This negative vacancy parameter dominates the excess

Cr^{3+} replaced with the Co^{2+} and these excess ions are not too high, so no impurity peaks have been observed in the XRD patterns. A slight distortion of inverse spinel structure has been confirmed from the tolerance factor for all samples of both series. The dominance of Cr^{3+} with extra Co^{2+} ions due to lowering the packing fraction demonstrates strongly increasing trend of vacancy parameter with increase of Cr^{3+} and leading to transform semiconducting to metallic behavior in S2 series. However, a single phase cubic structure is observed for the samples of S2 series without any impurity peak in the XRD patterns. The observed anion displacement for the samples of two series are dominated by the deviation of oxygen positional parameters from their standard value of 0.375. Expansion of lattice volume for the series S1 has been observed due to the larger ratio of Cr^{2+}/Co^{2+} at tetrahedral site than the Cr^{3+}/Co^{2+} ratio at octahedral site. In S2 series, Fe^{3+} has been replaced by Cr^{3+} with a simultaneous addition of Co^{2+}, resulting an increase in lattice volume. In series S1, both the d_x and d_B show a decreasing trend, which may be attributed to the increase of Cr^{3+} with a lower density of 7.14 g cm^{-3} than that of Co^{2+} (8.9 g cm^{-3}).[45] Although pelletization pressure and sintering temperature for all samples were the same, there is an increasing trend of ductility with an increase of Cr content. At higher sintering temperature (>1100 °C) the ductility of Cr/Cr-based alloys and composite is reported to improve.[46]

In series S2, Cr metal having lower density replaced the Fe (7.87 g cm^{-3}) with slightly higher density.[45] However, addition of same amount of Co metal with high density, resulted in the increasing trend of d_B, and d_x with a increase in porosity. However, the ductility is found to decrease possibly due to excess Co^{2+}. In addition, an increase of excess Co with lower shear modulus presumably plays a prominent role in lowering the ductile nature for the sample series S2. The decreasing trend of ductility as a function of Cr content are observed due to the increase of the Cr^{3+}/Fe^{2+} ratio. In series S1, the θ_D shows an increasing trend due to the greater θ_D of Cr than that of Co.[47] In series S2, the θ_D increases at lower Cr content (=0.125) but at a higher Cr content (>0.125), θ_D decreases due to the increase of Co/Cr ratio, and decrease of Fe/Cr ratio.

5. Conclusions

Two series of Cr^{3+} substituted cobalt ferrite with stoichiometric (S1 series) and non-stoichiometric (S2 series) ratios have been synthesized by the standard solid-state reaction technique. XRD patterns for all samples of both series indicate a single phase cubic spinel structure with a space group of $Fd\bar{3}m$. FTIR spectra of the synthesized samples also confirm the spinel structure. The cation distribution calculated from the extracted Rietveld refined data confirms the mixed spinel structure of all samples of both series. In both the stoichiometric and non-stoichiometric series, an enhancement of lattice parameter have been found. From the analysis of elastic properties, it is found that all the samples for both series are ductile in nature. For the stoichiometric series Cr^{3+} together with Co^{2+} is assumed to have influenced the structural and mechanical properties. In addition, non-stoichiometric compositions provide an opportunity to tailor Co^{2+}/Cr^{3+} and Fe^{3+}/Cr^{3+} in the inverse spinel ferrite which causes the defect in structure, and modification of mechanical behavior.

6 Appendix-A

Equations belonging to Section 3:

Equation for theoretical lattice parameter:[1]

$$a_{th} = \frac{8}{3\sqrt{3}}\left[(r_{tet} + R_O) + \sqrt{3}\,(r_{oct} + R_O)\right] \quad \text{(A1)}$$

where R_O (=1.32 Å) is the ionic radius of oxygen.

The N–R function is as follows:[17]

$$F(\theta) = \left[\frac{1}{2}\left(\frac{\cos^2\theta}{\sin\theta} + \frac{\cos^2\theta}{\theta}\right)\right] \quad \text{(A2)}$$

The lattice parameter for each Bragg position:[30]

$$a_{hkl} = d_{hkl}\sqrt{h^2 + k^2 + l^2} \quad \text{(A3)}$$

Here, a_{hkl}, d_{hkl} are the lattice constant and interplanar spacing respectively.

Equations for bulk density $d_B$and X-ray density d_x[32]

$$d_B = \frac{m}{V_{geo}} = \frac{m}{\pi\left(\frac{d}{2}\right)^2 \times t} \quad \text{(A4)}$$

$$d_x = \frac{8M}{N_A {a_{exp}}^3} \quad \text{(A5)}$$

Equation for porosity:[8]

$$P\% = \left(1 - \frac{d_B}{d_x}\right) \times 100 \quad \text{(A6)}$$

where M is the molecular mass calculated from molecular formulae, a_{exp} is the experimental lattice constant and N_A (=6.02 × 10^{23}) is Avogadro's number.

Equation for oxygen positional parameter u:[1]

$$u = \left[\left(\frac{r_{tet} + R_O}{\sqrt{3}a}\right) + 0.25\right] \quad \text{(A7)}$$

Stanley's equations:[1]

$$L_A = \frac{a\sqrt{3}}{4}, \text{ and } L_B = \frac{a\sqrt{2}}{4} \quad \text{(A8)}$$

The equations for tetrahedral and octahedral bond lengths (d_{AL}) and (d_{BL}), tetrahedral edge length (d_{AE}), and shared (d_{BE}) and un-shared octahedral edge lengths (d_{BEU}) are as follows:[1]

$$d_{AL} = a\sqrt{3}(u - 0.25) \quad \text{(A9)}$$

$$d_{BL} = a\sqrt{3u^2 - \frac{11}{4}u + \frac{43}{64}} \quad \text{(A10)}$$

$$d_{AE} = a\sqrt{2}(2u - 0.5) \quad \text{(A11)}$$

$$d_{BE} = a\sqrt{2}(1-2u) \quad \text{(A12)}$$

$$d_{BAU} = a\sqrt{4u^2 - 3u + \frac{11}{16}} \quad \text{(A13)}$$

Equations for various bond length and bond angles:[1]
Me–Me distances

$$b = \frac{a\sqrt{2}}{4} \quad \text{(A14)}$$

$$c = \frac{a\sqrt{11}}{8} \quad \text{(A15)}$$

$$d = \frac{a\sqrt{3}}{4} \quad \text{(A16)}$$

$$e = \frac{3\sqrt{3}a}{8} \quad \text{(A17)}$$

$$f = \frac{a\sqrt{6}}{4} \quad \text{(A18)}$$

Me–O distances

$$p = a\left(\frac{5}{8} - u\right) \quad \text{(A19)}$$

$$q = a\sqrt{3}\left(u - \frac{1}{4}\right) \quad \text{(A20)}$$

$$r = \frac{a\sqrt{11}u}{4} \quad \text{(A21)}$$

$$s = a\sqrt{3}\left(\frac{u}{3} + \frac{1}{8}\right) \quad \text{(A22)}$$

Bond angles

$$\theta_1 = \cos^{-1}\left(\frac{p^2 + q^2 - c^2}{2pq}\right) \quad \text{(A23)}$$

$$\theta_2 = \cos^{-1}\left(\frac{p^2 + r^2 - e^2}{2pr}\right) \quad \text{(A24)}$$

$$\theta_3 = \cos^{-1}\left(\frac{p^2 - b^2}{2p^2}\right) \quad \text{(A25)}$$

$$\theta_4 = \cos^{-1}\left(\frac{p^2 + s^2 - f^2}{2ps}\right) \quad \text{(A26)}$$

$$\theta_5 = \cos^{-1}\left(\frac{r^2 + q^2 - d^2}{2qr}\right) \quad \text{(A27)}$$

Equations for the ionic packing coefficient P_{tet} and P_{oct} at the tetrahedral and octahedral sites:[34]

$$P_{tet} = \frac{R_{tet} - R_O}{r_{tet}} \quad \text{(A28)}$$

$$P_{oct} = \frac{R_{oct} - R_O}{r_{oct}} \quad \text{(A29)}$$

Here, R_{tet} (=d_{AL}) and R_{tet} (=d_{BL})are the average bond length at tetrahedral and octahedral sites respectively.

Equation for the fulfillment coefficient (α) of the unit cell using the following relation:[34]

$$\alpha = \frac{32\pi\left({r_{tet}}^3 + 2{r_{oct}}^3 + 4{R_O}^3\right)}{3{a_{exp}}^3} \quad \text{(A30)}$$

Equation of vacancy parameter β:[34]

$$\beta = \frac{{a_{th}}^3 - {a_{exp}}^3}{{a_{th}}^3} \times 100\% \quad \text{(A31)}$$

Equation for tolerance factor calculation:[36]

$$T = \frac{1}{\sqrt{3}}\left[\frac{r_{tet} + R_O}{r_{oct} + R_O}\right] + \frac{1}{\sqrt{2}}\left[\frac{R_O}{r_{tet} + R_O}\right] \quad \text{(A32)}$$

The FWHM data has been calculated by using the following relation:[37]

$$\beta_O = 0.5346 \times W_L + \sqrt{0.2166{W_L}^2 + {W_G}^2} \quad \text{(A33)}$$

Here, β_O is observed FWHM, W_L, and W_G is the Lorentzian and Gaussian width respectively. The instrumental broadening (β_i) removal equation:[34]

$$\beta_{hkl} = [(\beta_O - \beta_i)({\beta_O}^2 - {\beta_O}^2)^{0.5}]^{0.5} \quad \text{(A34)}$$

The Scherrer equation:[17]

$$D = \frac{0.9\lambda}{\beta_{311}\cos\theta} \quad \text{(A35)}$$

Here, β_{311} is the FWHM at (311) plane (most intense peak), λ (=1.5406 Å) represents the wavelength of incident X-rays.

Modified Scherrer equation:[22]

$$\ln\beta = \ln\left(\frac{0.9\lambda}{D}\right) + \ln\left(\frac{1}{\cos\theta}\right) \quad \text{(A36)}$$

Williamson–Hall relation:[14,21]

$$\beta_{tot} = \beta_{strain} + \beta_{crystal} = 4\varepsilon\tan\theta + \frac{0.9\lambda}{D\cos\theta}$$

or,

$$\beta_{hkl}\cos\theta = 4\varepsilon\sin\theta + \frac{0.9\lambda}{D} \quad \text{(A37)}$$

Here, β_{hkl} is the total broadening due to strain and size in a particular peak having the (hkl) value which is written exchange of β_{tot}.

Equation for the size strain plot:[21]

$$(d_{hkl}\beta_{hkl}\cos\theta)^2 = \frac{K\lambda}{D}\left(d_{hkl}{}^2\beta_{hkl}\cos\theta\right) + \frac{\varepsilon^2}{4} \quad \text{(A38)}$$

Here, d_{hkl} is lattice spacing for different (hkl) planes.

Force constant according to Waldron relation:[21]

$$k_t = 4\pi^2 c^2 \nu_1{}^2 \mu \quad \text{(A39)}$$

$$k_o = 4\pi^2 c^2 \nu_2{}^2 \mu \quad \text{(A40)}$$

$$k_{av} = (k_t + k_o)/2 \quad \text{(A41)}$$

Here, c is the velocity of light, μ is the reduced mass which we have calculated by the following relation:[38,39]

$$\mu = \frac{m_1 \times m_2}{m_1 + m_2} \quad \text{(A42)}$$

where m_1 is the weighted average of atomic weights of the cations residing at the A-site or B-site while m_2 is the atomic weight of oxygen anion.

Equation for the stiffness constant C_{11}, C_{12}:[21]

$$C_{11} = \frac{k_{av}}{a} \quad \text{(A43)}$$

$$C_{12} = \frac{\sigma C_{11}}{1-\sigma} \quad \text{(A44)}$$

Here, σ is the Poisson's ratio as a function of pore fraction P. The corresponding relation for σ is as follows:[21]

$$\sigma = 0.324(1 - 1.043P) \quad \text{(A45)}$$

Some elastic properties related equations:[40,41]

Bulk modulus:

$$B = \frac{1}{3}(C_{11} + 2C_{12}) \quad \text{(A46)}$$

Longitudinal wave velocity,

$$v_l = \sqrt{\frac{C_{11}}{d_x}} \quad \text{(A47)}$$

Here, d_x is the X-ray density.

Transverse wave velocity,

$$v_t = \frac{v_l}{\sqrt{3}} \quad \text{(A48)}$$

Rigidity modulus,

$$G = d_x v_t{}^2 \quad \text{(A49)}$$

Young's modulus,

$$E = 2(1 + \sigma)G \quad \text{(A50)}$$

Mean velocity,

$$v_m = \left(\frac{1}{3}\left(\frac{2}{v_t{}^3} + \frac{1}{v_l{}^3}\right)\right)^{-1/3} \quad \text{(A51)}$$

Hasselman and Fularth's formulae for the corrected zero porosity elastic moduli:[21,41]

$$\frac{1}{E_0} = \frac{1}{E}\left[1 - \frac{3p(1-\sigma)(9+5\sigma)}{2(7-5\sigma)}\right] \quad \text{(A52)}$$

$$\frac{1}{G_0} = \frac{1}{G}\left[1 - \frac{15p(1-\sigma)}{7-5\sigma}\right] \quad \text{(A53)}$$

$$B_0 = \left[\frac{E_0 G_0}{3(3G_0 - E_0)}\right] \quad \text{(A54)}$$

$$\sigma_0 = \left(\frac{E_0}{2G_0}\right) - 1 \quad \text{(A55)}$$

Anderson's formula for the Debye temperature, θ_D:[44]

$$\theta_D = \frac{\hbar}{k_B}\left(\frac{3qd_x N_A}{4\pi M}\right)^{\frac{1}{3}} v_m \quad \text{(A56)}$$

where $\hbar$ is Planck's constant, k_B is Boltzmann's constant, N_A is Avogadro's number, d_x is the density, M is the molecular mass, and q is the number of atoms per unit formula.

Equations for thermal conductivity:[38]

$$K_{min} = k_B v_m \left(\frac{M}{qd_x N_A}\right)^{-2/3} \quad \text{(A57)}$$

7 Appendix B

Conflicts of interest

There is no conflicts to declare.

Acknowledgements

The authors are thankful to the Committee for Advanced Studies & Research (CASR), Grant No. 343(15), Bangladesh University of Engineering and Technology for the financial support of this research.

References

1 N. Amri, J. Massoudi, K. Nouri, M. Triki, E. Dhahri and L. Bessais, Influence of neodymium substitution on structural, magnetic and spectroscopic properties of Ni–Zn–Al nano-ferrites, *RSC Adv.*, 2021, **11**, 13256–13268.
2 S. Akhtar, Q. Khan, S. Anwar, G. Ali, M. Maqbool, M. Khan, S. Karim and L. Gao, A Comparative Study of the Toxicity of Polyethylene Glycol-Coated Cobalt Ferrite Nanospheres and Nanoparticles, *Nanoscale Res. Lett.*, 2019, **14**(1), 386.
3 S. Jauhar, J. Kaur, A. Goyal and S. Singhal, Tuning the properties of cobalt ferrite: a road towards diverse applications, *RSC Adv.*, 2016, **6**(100), 97694–97719.
4 S. K. Gore, S. S. Jadhav, V. V. Jadhav, S. M. Patange, M. Naushad, R. S. Mane and K. H. Kim, The structural and

magnetic properties of dual phase cobalt ferrite, *Sci. Rep.*, 2017, **7**(1), 2524.

5 S. Y. Srinivasan, K. M. Paknikar, D. Bodas and V. Gajbhiye, Applications of cobalt ferrite nanoparticles in biomedical nanotechnology, *Nanomedicine*, 2018, **13**(10), 1221–1238.

6 A. Hai, B. Alqassem, G. Bharath, K. Rambabu, I. Othman, M. A. Haija and F. Banat, Cobalt and nickel ferrites based capacitive deionization electrode materials for water desalination applications, *Electrochim. Acta*, 2020, **363**, 137083.

7 M. S. Shakil, M. A. Hasan, M. F. Uddin, A. Islam, A. Nahar, H. Das, M. N. I. Khan, B. P. Dey, B. Rokeya and S. M. Hoque, In Vivo Toxicity Studies of Chitosan-Coated Cobalt Ferrite Nanocomplex for Its Application as MRI Contrast Dye, *ACS Appl. Bio Mater.*, 2020, **3**(11), 7952–7964.

8 M. Z. Ahsan, M. A. Islam and F. A. Khan, Tunability of ac Conductivity in Manganese doped Cobalt ferrite Nanoparticles, *Results Phys.*, 2021, **21**, 103782.

9 M. Z. Ahsan, M. A. Islam, A. A. Bally and F. A. Khan, Spectroscopic analysis for electric and magnetic properties of manganese doped cobalt nanoferrite, *Results Phys.*, 2020, **17**, 103172.

10 M. Z. Ahsan, M. A. Islam and F. A. Khan, Effects of sintering temperature on ac conductivity, permittivity, and permeability of manganese doped cobalt ferrite nanoparticles, *Results Phys.*, 2020, **19**, 103402.

11 M. Z. Ahsan, F. A. Khan and M. A. Islam, Frequency and temperature dependent intrinsic electric properties of manganese doped cobalt ferrite nanoparticles, *Results Phys.*, 2019, **14**, 102484.

12 M. Z. Ahsan, F. A. Khan and M. A. Islam, Frequency and Temperature Dependent Dielectric and Magnetic Properties of Manganese Doped Cobalt Ferrite Nanoparticles, *J. Electron. Mater.*, 2019, **48**(12), 7721–7729.

13 M. Z. Ahsan and M. A. Islam, A Theoretical Approach: Effects of Mn Substitution in Cobalt Ferrite, *Am. J. Appl. Sci.*, 2019, **5**(3), 56–61.

14 G. Kumar, R. K. Kotnala, J. Shah, V. Kumar, A. Kumar, P. Dhiman and M. Singh, Cation distribution: a key to ascertain the magnetic interactions in a cobalt substituted Mg–Mn nanoferrite matrix, *Phys. Chem. Chem. Phys.*, 2017, **19**(25), 16669–16680.

15 P. Bera, R. V. Lakshmi, B. H. Prakash, K. Tiwari, A. Shukla, A. K. Kundu and H. Barshilia, Solution combustion synthesis, characterization, magnetic, and dielectric properties of $CoFe_2O_4$ and $Co_{0.5}M_{0.5}Fe_2O_4$ (M = Mn, Ni, and Zn), *Phys. Chem. Chem. Phys.*, 2020, **22**, 20087–20106.

16 R. Saravanan, *Ferrite Materials for Memory Applications*, Material research foundation, 2017, vol. 18, p. 29.

17 S. Debnath and R. Das, Cobalt doping on nickel ferrite nanocrystals enhances the micro-structural and magnetic properties: Shows a correlation between them, *J. Alloys Compd.*, 2020, 156884.

18 A. Monshi, M. R. Foroughi and M. R. Monshi, Modified Scherrer Equation to Estimate More Accurately Nano-Crystallite Size Using XRD, *World J. Nano Sci. Eng.*, 2012, **02**(03), 154–160.

19 D. Nath, F. Singh and R. Das, X-Ray Diffraction Analysis by Williamson-Hall, Halder-Wagner and Size-Strain Plot Methods of CdSe Nanoparticles- A comparative study, *Mater. Chem. Phys.*, 2019, 122021.

20 D. Bouokkeze, J. Massoudi, W. Hzez, M. Smari, A. Bougoffa, K. Khirouni and L. Bessais, Investigation of the structural, optical, elastic and electrical properties of spinel $LiZn_2Fe_3O_8$ nanoparticles annealed at two distinct temperatures, *RSC Adv.*, 2019, **9**(70), 40940–40955.

21 K. V. Chandekar and K. M. Kant, Size-strain analysis and elastic properties of $CoFe_2O_4$nanoplatelets by hydrothermal method, *J. Mol. Struct.*, 2018, **1154**, 418–427.

22 K. V. Chandekar, M. Shakir and S. AlFaify, A structural, elastic, mechanical, spectroscopic, thermodynamic, and magnetic properties of polymer coated $CoFe_2O_4$ nanostructures for various applications, *J. Mol. Struct.*, 2020, 127681.

23 H. L. Andersen, B. A. Frandsen, H. P. Gunnlaugsson, M. R. V. Jørgensen, S. J. L. Billinge, K. M. Ø. Jensen and M. Christensen, Local and long-range atomic/magnetic structure of non-stoichiometric spinel iron oxide nanocrystallites, *IUCrJ*, 2021, **8**(1), 33–35.

24 N. Kumar, R. K. Singh and H. K. Satyapal, Structural, optical, and magnetic properties of non-stoichiometric lithium substituted magnesium ferrite nanoparticles for multifunctional applications, *J. Mater. Sci.: Mater. Electron.*, 2020, **31**, 9231–9241.

25 E. E. Ateia, S. K. Abdel-Aal, K. Seham and A. Abd Allah, Synthesis and characterization of nonstoichiometric potassium/magnesium nanoferrites for multifunctional applications, *J. Mater. Sci.: Mater. Electron.*, 2017, **29**(2), 1–8.

26 Y. Xu, D. Sun, H. Hao, D. Gao and Y. Sun, Non-stoichiometric Co (ii), Ni (ii), Zn (ii)-ferrite nanospheres: size controllable synthesis, excellent gas-sensing and magnetic properties, *RSC Adv.*, 2016, **6**(101), 98994–99002.

27 I. C. Nlebedim, A. J. Moses and D. C. Jiles, Non-stoichiometric cobalt ferrite, CoxFe3−xO4 (x=1.0 to 2.0): Structural, magnetic and magnetoelastic properties, *J. Magn. Magn. Mater.*, 2013, **343**, 49–54.

28 C. Dun, G. Xi, Y. Zhang, X. Heng, Y. Liu, X. Xing and R. Liang, Magnetic and magnetostrictive properties of non-stoichiometric cobalt ferrite synthesized from spent Li-ion batteries, *J. Magn. Magn. Mater.*, 2020, 167185.

29 R. W. G. Wyckoff *Structure of Crystals The Chemical* Catalog Company, INC, New York, 2nd edn, 1931, p. 290.

30 S. M. Patange, S. E. Shirsath, S. S. Jadhav and K. M. Jadhav, Cation distribution study of nanocrystalline NiFe2−xCrxO4 ferrite by XRD, magnetization and Mössbauer spectroscopy, *Phys. Status Solidi A*, 2011, **209**(2), 347–352.

31 M. J. Iqbal and M. R. Siddiquah, Electrical and magnetic properties of chromium-substituted cobalt ferrite nanomaterials, *J. Alloys Compd.*, 2008, **453**(1–2), 513–518.

32 M. A. Rahman, M. T. Islam, M. S. J. Singh, M. Samsuzzaman and M. E. H. Chowdhury, Synthesis and characterization of Mg–Zn ferrite based flexible microwave composites and its application as SNG metamaterial, *Sci. Rep.*, 2021, **11**, 7654.

33 B. B. V. S. V. Prasad, Cation distribution, structural and electric studies on cadmium substituted nickel–zinc ferrite, *Mod. Phys. Lett. B*, 2014, **28**(19), 1450155.
34 K. A. M. Khalaf, A. D. Al-Rawas, H. M. Widatallah, K. S. Al-Rashdi, A. Sellai, A. M. Gismelseed and A. H. Al-Rajhi, Influence of Zn 2+ ions on the structural and electrical properties of Mg1−xZnxFeCrO4spinels, *J. Alloys Compd.*, 2016, **657**, 733–747.
35 T. Groń, Influence of vacancies and mixed valence on the transport processes in solid solutions with the spinel structure, *Philos. Mag. Lett.*, 1994, **70**(1), 121–132.
36 M. I. Arshad, S. Arshad, K. Mahmood, A. Ali, N. Amin, R. Umaid-ur and M. Ajaz-un Nabi, Impact of Mg doping on structural, spectral and dielectric properties of Cd–Cu nano ferrites prepared *via* sol-gel auto combustion method, *Phys. B*, 2020, 412496.
37 P. M. Shafi and A. Chandra Bose, Impact of crystalline defects and size on X-ray line broadening: A phenomenological approach for tetragonal SnO_2 nanocrystals, *AIP Adv.*, 2015, **5**, 057137.
38 K. B. Modi, S. J. Shah, N. B. Pujara, T. K. Pathak, N. H. Vasoya and I. G. Jhala, Infrared spectral evolution, elastic, optical and thermodynamic properties study on mechanically milled Ni0.5Zn0.5Fe2O4 spinel ferrite, *J. Mol. Struct.*, 2013, **1049**, 250–262.
39 N. Bouhadouza, A. Rais, S. Kaoua, M. Moreau, K. Taibi and A. &Addou, Structural and vibrational studies of NiAlxFe2−xO4 ferrites (0≤x≤1), *Ceram. Int.*, 2015, **41**(9), 11687–11692.
40 M.-M. Wu, L. Wen, B.-Y. Tang, L.-M. Peng and W.-J. Ding, First-principles study of elastic and electronic properties of $MgZn_2$ and $ScZn_2$ phases in Mg–Sc–Zn alloy, *J. Alloys Compd.*, 2010, **506**(1), 412–417.
41 D. P. H. Hasselman and R. M. Fulrath, Effect of Small Fraction of Spherical Porosity on Elastic Moduli of Glass, *J. Am. Ceram. Soc.*, 1964, **47**(1), 52–53.
42 Y. Pan and W. M. Guan, Probing the balance between ductility and strength: transition metal silicides, *Phys. Chem. Chem. Phys.*, 2017, **19**(29), 19427–19433.
43 S. A. B. I. N. Frantsevich and F. F. Voronov, *Elastic Constants and Elastic Moduli of Metals and Insulators Handbook*, I. N. Frant, Naukova Dumka, Kiev, 1983.
44 *Physics Acoustics*, ed. O. L. Anderson and W. P. Mason, Academic Press, New York, 1965, vol. 3B, pp. 43–95.
45 https://sciencenotes.org/density-elements-periodic-table/.
46 Y. F. Gu, H. Harada and Y. Ro, Chromium and chromium-based alloys: Problems and possibilities for high-temperature service, *JOM*, 2004, **56**(9), 28–33.
47 http://www.knowledgedoor.com/2/elements_handbook/debye_temperature.html.